




# Managing wind resource variation for rooftop turbine placement

Philipp Eppel<sup>1</sup>, Gitanjali Thakur<sup>2</sup>, and Debra F. Laefer<sup>3,a</sup> 

<sup>1</sup> Mechanical Engineering, Coburg University of Applied Sciences, Friedrich-Streib-Str. 2, 96450 Coburg, Germany

<sup>2</sup> School of Civil Engineering, University College Dublin, Newstead, Dublin 4, Belfield, Ireland

<sup>3</sup> Tandon School of Engineering, Center for Urban Science + Progress and Department of Civil and Urban Engineering, New York University, 370 Jay St. 1301C, Brooklyn, NY 11201, USA

Received 20 January 2022 / Accepted 29 March 2022 / Published online 2 May 2022

© The Author(s), under exclusive licence to EDP Sciences, Springer-Verlag GmbH Germany, part of Springer Nature 2022

**Abstract** Numerous localities have attempted to harness wind resources for electricity generation using roof-integrated wind turbines (RIWTs). Disappointingly, the monitored performance of RIWTs is typically only 5–11% of the designed capacity. Since direct wind measurement is expensive for micro-generation and simplified analytical methods are often insufficiently precise for complex geometries, poor outcomes are not surprising. To combat this, the current study explores the extent to which this deficit is due to poor RIWT placement in the absence of precise wind power information for installation sites and how this may be countered with terrestrial laser scanning-based models for complex structures. This is demonstrated with a cluster of complex suburban buildings with ground elevation changes of up to 4.2 m. Those data were used to populate a computational fluid dynamic model for detailed wind flow field simulation using a Navier–Stokes solver, ANSYS CFX. This approach demonstrated that wind power ranged from 0 to 100% of the capacity factor across the main study rooftop, representing the difference between cost recovery of a €16,500 RIWT in less than 1.5 years and a financially non-viable installation. This study provides a partial explanation for the disappointing results of RIWT installation, as well as a methodology to optimize RIWT placement to avoid non-viable installations and improve cost recovery period predictions.

## 1 Introduction

The prolonged use of fossil fuels will eventually lead to their depletion, as well as the affiliated degradation of the environment. Hence, interest continues to rise in renewable energy. For example, the European Union set a target of 32% electricity generation from renewable sources within the European states by 2030 [1]. Small-scale renewables (micro-generation) like roof-integrated wind turbines (RIWTs) could play an important role in reducing carbon monoxide emissions, however, RIWTs have failed to perform as expected. In fact, according to the Encraft Warwick Wind Trials Project, which investigated 168,950 h of operation of 26 roof mounted wind turbines from 5 UK manufacturers, the average capacity factor (CF) was only 4.15% [2]. Arguably, one reason for the wide gap between the promised output by the manufacturer and the electricity obtained by the consumer is the absence of precise wind resource information at the installation location [3]. In most cases, turbine output is predicted using a wind atlas for a region, which gives the average value of wind velocity and wind direction without explicitly considering the effects of a dense built environment coupled with vege-

tation. However, in such a complex environment, wind flow is unsteady and non-uniform in both the horizontal and vertical directions, which can massively impact the output of an RIWT depending upon its location within the wind field. In terms of predicting this inconsistent flow, wind tunnel studies have demonstrated an error rate of only 5% in homogenous urban areas, but in heterogeneous areas, the error rate climbed to 20% [4].

## 2 Project scope

The goal of this work was to explore barriers to optimal RIWT installation in a local context and provide recommendations for improved outputs. A previous study conducted in Dublin, Ireland endeavored to model wind resources over the urban environment but ultimately identified a remaining gap in determining wind resource conditions between the inertial sub-layer and the city surface [5]. Thus, to better understand the problem in this critical layer where most RIWTs are installed, a specific building was chosen for direct investigation at the city surface level. The Roe-buck Hall Residence, located on the University College

<sup>a</sup> e-mail: [debra.laefer@nyu.edu](mailto:debra.laefer@nyu.edu) (corresponding author)

**Fig. 1** Study site with the main study building shown as Building 4)

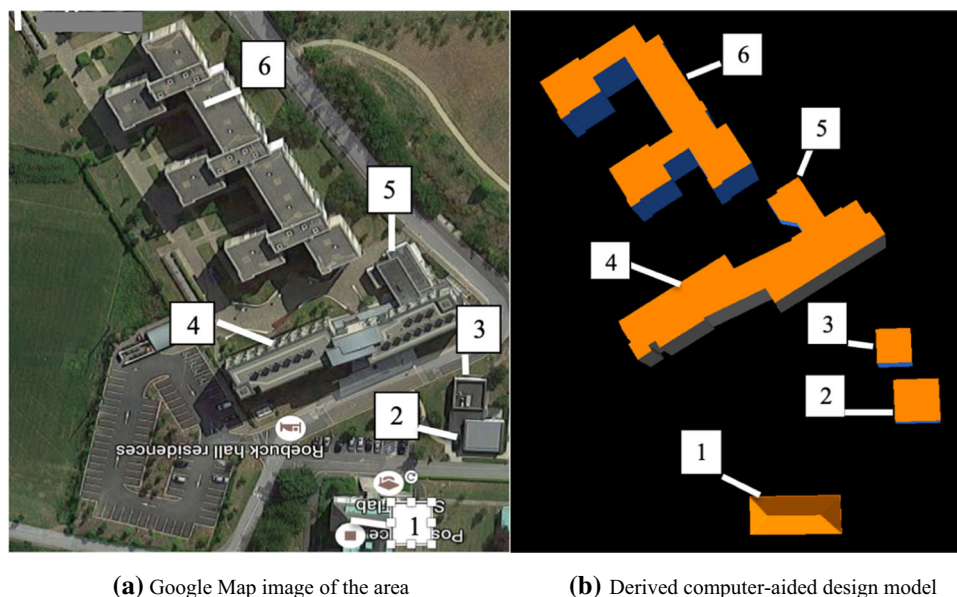


**Fig. 2** Roebuck hall residence (Building 4) on the university college of Dublin's campus

Dublin's campus was chosen as the locus of investigation. The building was selected as it was the focus of an on-campus effort to construct a zero-carbon structure, although an RIWT was never part of the design. The building, herein referred to as Building 4, has 6 stories, is 19.6 m in height, and can be characterized as being in a moderately dense environment, composed of a cluster of 6 multi-story buildings (Figs. 1, 2), thus providing a level of complexity typically unexplored in desk studies. To facilitate the exploration of this real study area, Dublin's wind climate was also analyzed more generally using meteorological data to assess its suitability for urban, micro-generation of electricity.

### 3 Methodology

Due to the heterogeneous nature of urban terrains, wind characteristics are very local. To estimate the available resources, a computational fluid dynamics (CFD) analysis was performed for the abovementioned site.

In contrast to the detailed CFD simulation in small structures, as shown in [6], where a Lattice Boltzmann code was used, in this work, a detailed CFD simulation around very large structures was performed with the commercial Navier–Stokes solver ANSYS CFX. This analysis required wind data (mean velocity and direction) and a geometrical model, on the basis of which a flow domain and grid were generated. The data were then pre-processed with the boundary conditions, and a physical model was selected. This preparatory work was followed by the CFD result analysis itself. Previous application of CFD to RIWT performance has been relatively limited and most narrow in scope. For example, Larin et al. [7] considered only a single, generic free-standing building on a symmetrical plane. The work by Ledo et al. [8] on houses with different roof profiles showed that on flat roofs wind accelerated independently of the wind direction. Balduzzi et al. [9] used two-dimensional (2D) simulations to investigate the influence of the installation's site on the potential energy yield. They performed a parametric analysis of flow around simplified, rectangular buildings and concluded that in urban areas RIWT installation should occur on structures significantly higher than the surrounding buildings, though how much higher was not quantified. Yang et al. [10] analyzed wind power generation in a dense urban area and demonstrated that upstream high-rise buildings had high detrimental impacts to the incoming wind resource and induced higher turbulence intensity over certain areas of the objective building. Wang et al. [11] analyzed wind energy over the roof top of cuboid buildings. They showed that buildings with smaller footprints had more wind energy density than those with larger footprints, irrespective of the length to width ratio of the roofs. Abohela et al. [12] showed that for 7 roof geometries (e.g., flat, gabled, domed) that the region of maximum turbulence intensity extends from directly above the roof to a distance of 1.3H. The scope of research herein

is significantly more complicated with respect to the inclusion of multiple structures, the level of detail representation included and the incorporation of variability in the terrain, thereby, challenging previous modeling assumptions.

For RIWT assessment, the wind power density across Building 4’s rooftop was mapped from the CFD results to investigate RIWT placed and estimate the electrical power that could be generated. Using a sophisticated CFD simulation of the cluster of structures and the variation, as well as more realistic building geometry than is typically included, other important information could also be extracted from these results. Two examples are given at the end of this work. The first involves analysis at 2 m above ground level to check for excessive wind velocities (e.g., at building corners) for pedestrian wind comfort. The second includes the aerodynamic forces (horizontal and vertical) on each of the buildings as needed for structural building design. The forces were computed with RANS CFD simulations, which delivered average aerodynamic loads (as described in Sect. 4.4). While load oscillations can be obtained with transient simulations, this was out of scope for this work, since RANS simulations deliver average loads, and they already give the correct orders of magnitude.

### 3.1 Wind data

The initial wind data for the site in Dublin, Ireland were obtained from the closest meteorological station, which is located at the Dublin airport (53° 25’34.39” N, 6°15’33.70” W). The station is situated on flat, open land sloping away gradually on the east side towards the Dublin coast, approximately 8 km away from the study site. The anemometer located there is positioned at a height of 10 m. The measured data represents the wind entering the city. For the analysis time series, two years of wind data was used. A mean wind speed of 6.31 m/s at an elevation of 10 m was calculated based on meteorological data. The dominant wind direction was from west, as shown in the wind rose in Fig. 3. As wind enters the city, its velocity changes due to interactions with the surface terrain. Thus, the use of raw meteorological data for an urban location is injudicious. Furthermore, direct measurement as currently obtained through a series of limited discrete collection points is expensive, time consuming, and delivers only a rather limited portion of the data set of the flow field on a single building. In contrast, CFD simulation can give realistic and extensive results, if used properly and with sufficient input geometry. To achieve this, a systematic approach is required to collect and process the input data and create the model, as discussed in the next sections.

### 3.2 Theoretical background: wind characteristics

To set the proper boundary conditions, perform post-processing, and interpret the results, knowledge of the

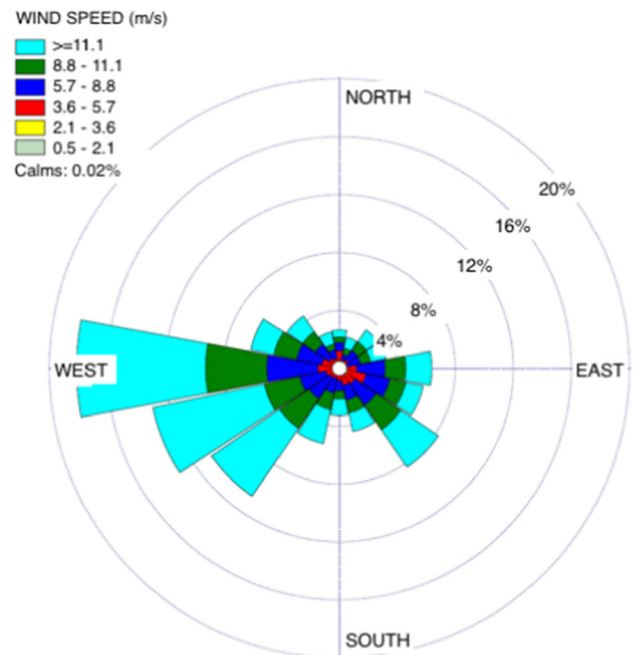


Fig. 3 Wind rose plot for dublin airport data

theoretical wind characteristics is needed. To properly position the boundary conditions sufficiently far from the buildings, the velocity profile away from the buildings must be known. Theoretically, the wind velocity within the neutral atmospheric boundary increases logarithmically with height (e.g., Gasch and Twele [13]) as per the following equation:

$$u(z) = \frac{u^*}{\kappa} \ln\left(\frac{z}{z_0}\right), \tag{1}$$

where  $u(z)$  is the average wind speed at a height  $z$ (m) above the ground,  $u^*$  is the friction velocity (m/s),  $\kappa$  is the von Karman constant ( $\sim 0.41$ ), and  $z_0$  is the roughness length (m). The roughness length is the height where the wind velocity decreases to zero following a logarithmic law. The friction velocity  $u^*$  relates to the wall shear stress  $\tau_w$  as per the following equation:

$$u^* = \sqrt{\tau_w/\rho}, \tag{2}$$

where  $\rho$  is the air density. Since neither the wall shear stress  $\tau_w$  nor the friction velocity  $u^*$  are known in advance, Eq. 1 is usually evaluated at two different heights ( $z_1$  and  $z$ ) and solved for  $u(z)$  as per the following equation:

$$u(z) = u(z_1) \frac{\ln(z/z_0)}{\ln(z_1/z_0)}. \tag{3}$$

To avoid the singularity in  $(z/z_0)$  at  $z=0$ , Eq. 3 must be modified to the following equation as per Gasch and

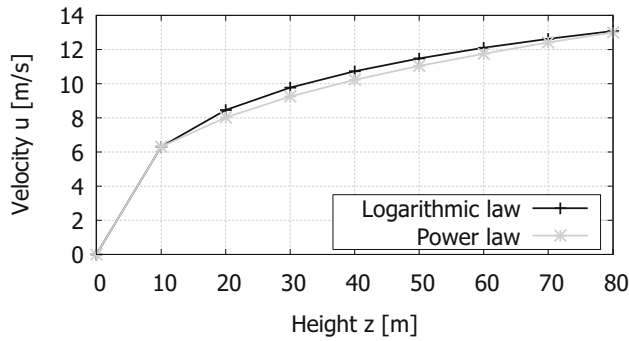


Fig. 4 Logarithmic and power law velocity profiles

Twele [13] and Ramponi et al. [14]:

$$u_{\log}(z) = u(z_1) \frac{\ln(z/z_0 + 1)}{\ln(z_1/z_0)}. \tag{4}$$

This velocity profile is then calibrated with the roughness length  $z_0$  and a velocity of  $u(z_1)$ . In an urban area,  $z_0$  can be taken to be 2 m as per Gasch and Twele [13]. The velocity profile can also be represented with the power law in the following equation, as per Tominaga and Blocken [15] and Masters [16]:

$$u_{\text{power}}(z) = u(z_1) \left(\frac{z}{z_1}\right)^\alpha, \tag{5}$$

where  $\alpha$  is the friction coefficient and is related to the ground roughness. The power law is useful to establish theoretical wind power computations. With the values  $z_0 = 2$  m,  $z_1 = 80$  m,  $u_1 = 13$  m/s,  $z_2 = 10$  m,  $u_2 = 6.31$  m based on measurements at Dublin airport meteorological station, the friction coefficient was computed as  $\alpha = 0.3473$ . These two velocity profiles compare well (Fig. 4).

For a constant velocity of  $u_0$ , the power available from the wind passing through a given area  $A$  is given by the following equation (e.g., Gasch & Twele [13]):

$$P_{\text{wind}} = \frac{1}{2} \dot{m} U_0^2 = \frac{1}{2} \rho A U_0^3. \tag{6}$$

However, since the velocity near the ground is not constant, the wind power through a vertical surface  $A$  is obtained by integration as per the following equation:

$$P_{\text{wind}} = \frac{1}{2} \rho \iint_A u(z)^3 dA. \tag{7}$$

By substituting Eq. 5 into Eq. 7, the theoretical power contained in the wind near the ground can be obtained. The wind turbine extracted power is then

$$P_{\text{turbine}} = c_p P_{\text{wind}}, \tag{8}$$

where  $c_p$  is the power coefficient. Betz [17] showed the maximum possible value as  $c_p = 16/27$ , but actual turbines extract less of the available wind power and fail to operate at this Betz limit [17].

Since the wind power is proportional to the wind speed cubed, minor inaccuracies in predicting the wind speed can lead to significant errors in the estimated energy yields. To address this and because of the transient characteristics of the wind, probabilistic approaches are generally used for wind energy prediction [13]. The Weibull distribution function is commonly employed for modeling the wind distribution [18–21]. For wind velocity distributions, the Rayleigh distribution, as per the following equation:

$$f(u) = \frac{\pi}{2} \left(\frac{u}{c}\right) \exp\left[-\frac{\pi}{4} \left(\frac{u}{c}\right)^2\right], \tag{9}$$

fits the wind velocity probability density function very well. By applying the Rayleigh distribution to the wind power one can show Eq. 11 as per Masters [16] and Mohammadi et al. [22]

$$\bar{P}_{\text{wind}} = \frac{6}{\pi} \frac{1}{2} \rho A \bar{U}_0^3, \tag{10}$$

where the bar indicates that these are mean quantities. In this work, no wind oscillations are considered in the numerical simulations, but through Eq. 10 one can see that these oscillations during the year will increase the available power by a factor of  $6/\pi$ .

### 3.3 Numerical simulation

To investigate the wind characteristics, especially the power density availability around the building complex, numerical simulations were performed with the solver ANSYS CFX. For that purpose, a geometrical model (i.e., a CAD model) was generated based on terrestrial laser scanner data. For the CFD simulations, best practice guidelines [23] were observed.

### 3.4 The geometrical model

In the absence of measured drawings, a Leica ScanStation P20 terrestrial scanner [24] was used to obtain a point cloud from which the building and site geometry were extracted (Fig. 5). The scanning was done in two phases. First, data were gathered from the ground with the assistance of four targets to aid with scan co-registration. Subsequently the scanner was placed on the roof of Building 4 to obtain information about the surrounding buildings and the terrain. In this way, the model also considered the various base elevation levels of the buildings, as captured in the point cloud—something not typically factored into wind analyses. The data were processed manually in the software programs Cyclone [25] and Cloudworx [26], which enabled manipulation of the point cloud data and export of the information into a CAD compatible model. The

**Fig. 5** Visualization of input data and derived geometric models

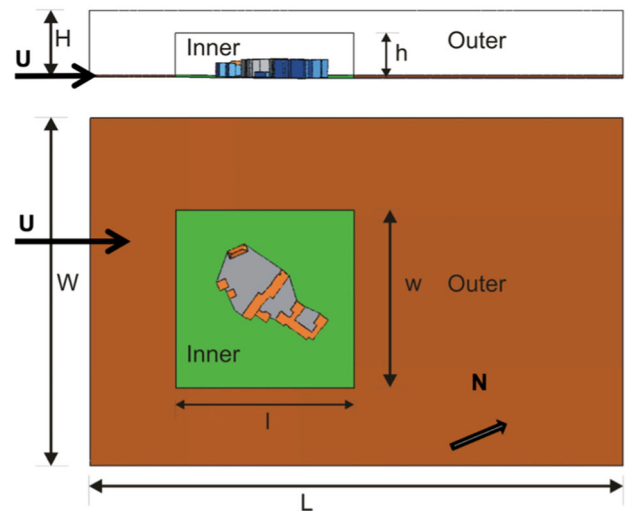
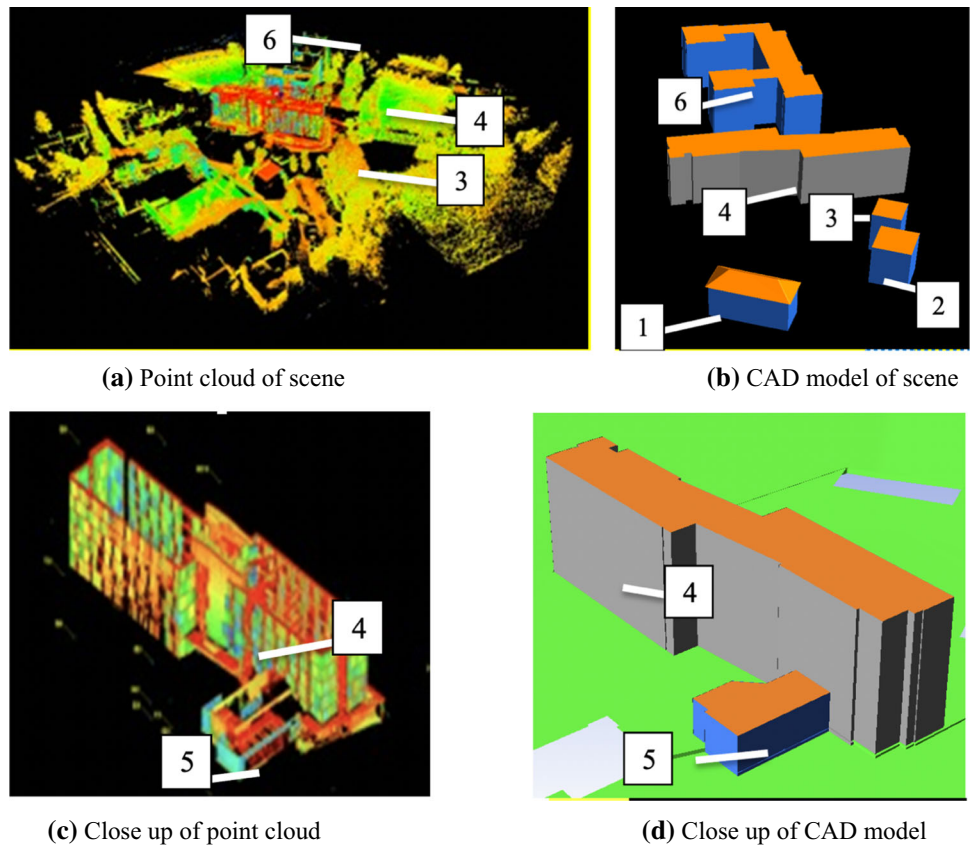


**Fig. 6** Computational domain (with wind shown from the left)

result can be considered a level of detail 2 representation, where the building footprints and profiles are accurately represented and the roofs are portrayed in a simplified manner. As will be further explored in the discussion section of this paper, this along with the realistic ground terrain is significantly more detailed than in most wind simulation models.

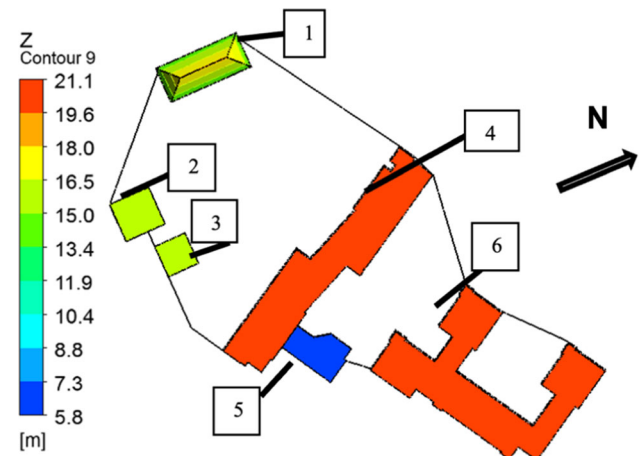
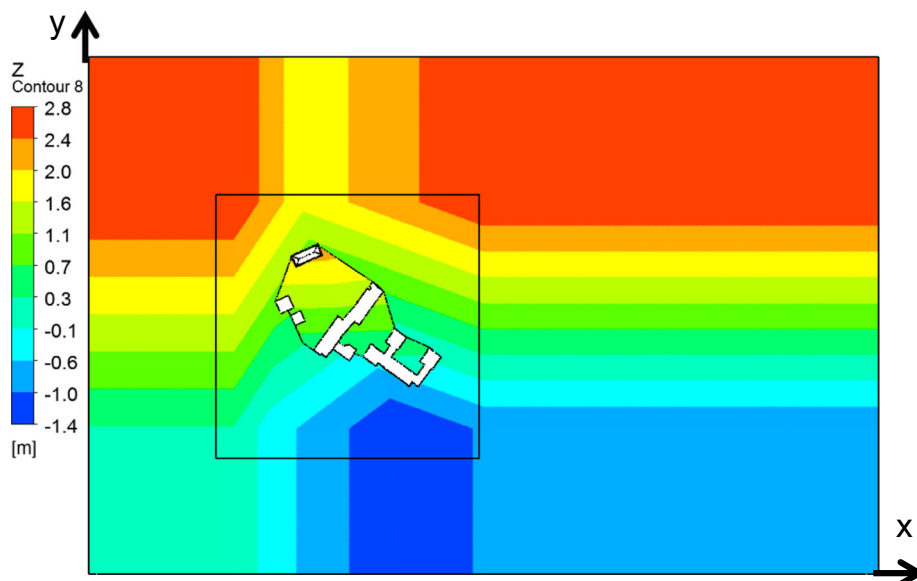


**Fig. 7** Building heights

### 3.5 Computational domain

To perform the numerical computations, a large computational domain was generated. This domain was divided in two subdomains: inner and outer (Fig. 6). The outer computational domain dimensions were selected as length,  $L=600$  m, height,  $H=75$  m, and width,  $W=400$  m. The inner computational domain had a length,  $l=200$  m, height,  $h=50$  m, and width,  $w=200$  m. The buildings were placed at the center of the inner domain. The heights of the buildings were as shown in Fig. 7:  $h_1 = 18$  m,  $h_2 = 16$  m,  $h_3 = 16$  m,

**Fig. 8** Ground level contours of the computational domain



$h_4 = 21.1$  m,  $h_5 = 7.3$  m and  $h_6 = 21.1$  m. The ground level of the computational domain varied from  $z=-1.4$  m to  $z=2.8$  m (Fig. 8). The three-dimensional model is shown in Fig. 9.

Tominaga et al. [27] suggested using a flow domain height five times or more the height of the tallest building. However, Tominaga et al. [27] assumed lateral and upper walls that were inviscid (i.e., free slip walls). In contrast, in this work, the opening boundary conditions from ANSYS CFX were adopted for the lateral and upper walls, as well as for the outlet. These involve a pressure boundary condition allowing inflow and outflow and, hence, the streamlines naturally curve around the buildings from which very good results can be achieved with a computational domain height of less than three times the height of the tallest building. In a preliminary study, the authors investigated the flow around a single rectangular building, showing that a flow domain with 5 times the height of the building and free slip walls deliver the same result as a flow domain with 3 times the height of the building with opening boundary condition.

As shown in Fig. 10, using a free slip wall or an opening on a domain seven times the height of the building (7H) showed no relevant impact on the velocities and forces on the building. At only three times the height of the building (3H) the free slip wall was negatively impacted the results, but this did not occur at 3H with the opening boundary conditions. Specifically, the left images show the free slip wall. For the 7H high flow domain (top left) the difference is irrelevant for the application, but for the lower flow domain (bottom left), the free slip wall improperly squeezes the flow, which leads to greater velocities on the top of the building and, hence, an over estimation of the available wind power. Additionally, at the top, the free slip wall boundary condition overly flattens the stream lines. These problems do not appear in the opening boundary condition cases (Fig. 10b,d). In both of those (7H and 3H), the velocity and streamline curvatures, and major dimensions of the

vortices match. The vortex flickers, as it is transient in nature and is, thus, captured in just an instant in time. These results are also confirmed when evaluating the drag force on the building (Fig. 11). Specifically, the 3H free slip wall (1-FSW 3H) visibly overestimates the force on the building for this reason.

The velocity profile above Building 4's center was also compared (Fig. 12). Here the velocity profile is also well reproduced by at 3D for the opening boundary condition. At a height up to 10 m, which is twice the height of the building, the velocity profile agrees well with 7H results for both the free slip wall (FSW 7H) and the opening boundary condition case (Opening 7H). Hence, with this flow domain (Opening 3H), the wind power available at the roof top of a building can be determined.

Since the grid around the building complex on this study is huge and the results of interest are mainly close to the roof of Building 4, 3H with an open boundary condition was selected based upon the preliminary results shown in Figs. 9–12. This enables the ability to generate a much finer mesh at the inner region around the buildings, thereby assuring more accurate results in the region of interest.

### 3.6 Computational grid

Of the two subdomains in the computational domain, the outer domain posed only a limited number of difficulties with regard to meshing and irregular ground conditions (as established from the measured data). In contrast, the inner domain posed additional difficulties due to the numerous irregular geometrical details of the buildings. These caused both meshing and resolution problems. To overcome these issues, more than 30 unstructured tetrahedral grids were generated and simulated as a grid study. The tetrahedral mesh was chosen since it was the only one able to accommodate the complexity and irregularities on the ground and

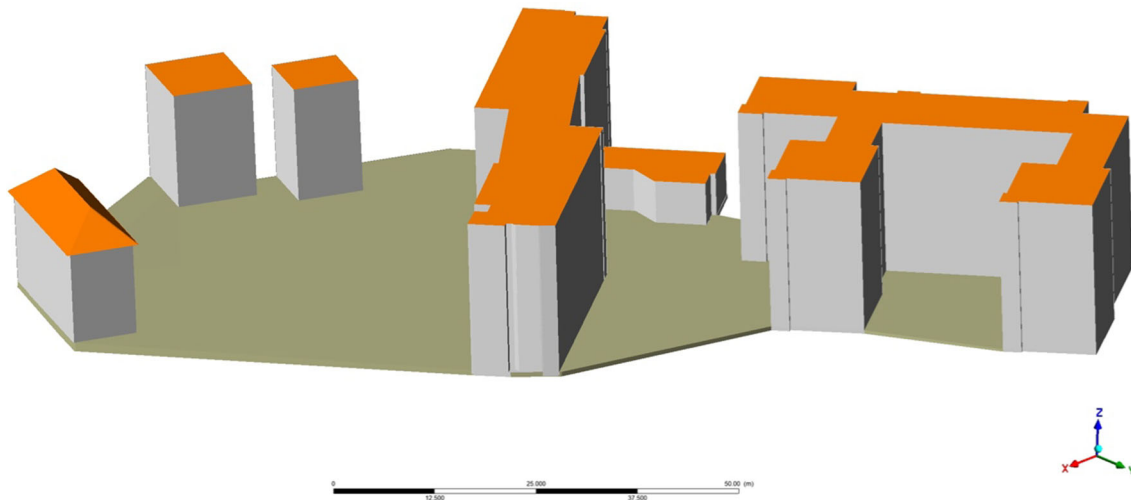


**Fig. 9** Three-dimensional view of close up of computational model

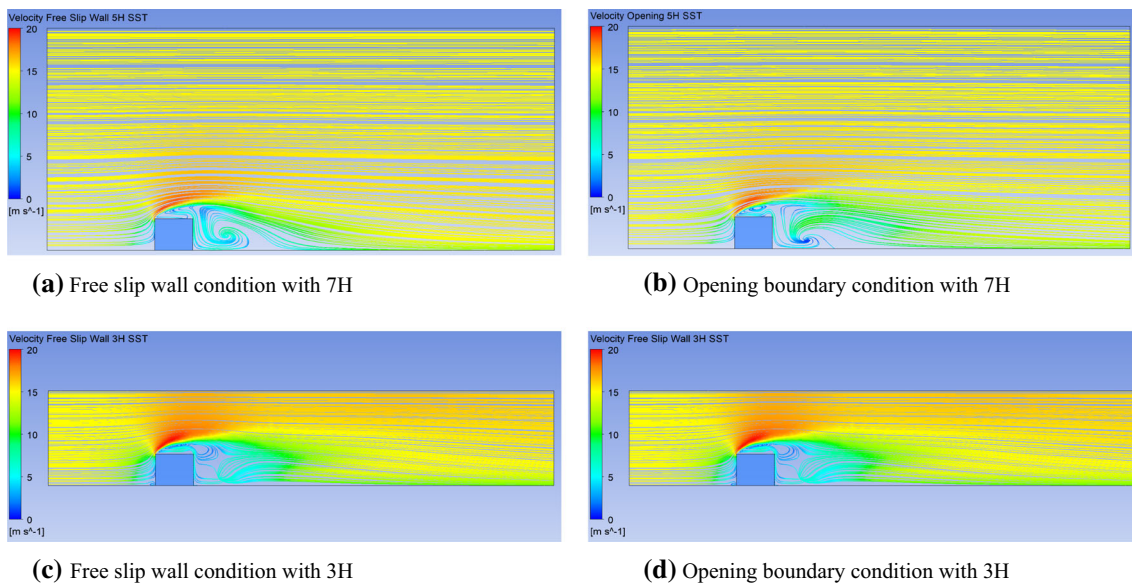


**Fig. 10** Comparison of results of flow domain five (7H, top images) and three (3H, bottom images) times the height of the building with free slip wall (left images) and opening (right images) boundary conditions

around the buildings. The geometry obtained by terrestrial laser scanning is very realistic and, hence, also complex. Tetrahedral meshes are very well integrated in ANSYS CFX and deliver highly reliable and accurate results. They are also the mesh elements recommended for complex geometries, as is the case for the geometry investigated in this work.

A total of 30 mesh sizes were investigated ranging from 1.2 to 28.5 million elements (Fig. 13). The results from the grids with more than 5 million elements delivered the same results in the large scale (grid independency). The parameter observed to assure the grid independency was the horizontal force on the roof of the Building 4, which is the building around and on top of which the flow was mainly to be investigated (Fig. 12). Since the size of the flow domain is very large, the maximum number of elements with respect to the capacity of the available hardware was determined to be 16 mil-

lion elements. The maximum viable number of elements was employed to maximize the greatest number of small details and resolve the flow around them. Specifically, the inner domain was meshed at a much finer resolution, resulting in about four times the number of elements compared to the outer domain, despite its much smaller volume. At the ground and on the roofs, 30 prism layers were generated. The aim was to achieve grid independency for the solution and proper grid resolution at locations throughout the computational domain. The grid sizes of the grid sensitivity study ranged from 1 to about 16 million elements. The mesh size and the prism layers are described in Table 1. Overviews of the tetrahedral grids and the prism layers are depicted in Figs. 14–17.

To verify the quality of the grid, the skewness of the tetrahedral cells was verified. The result is shown in Fig. 14. One can see that the quality ranges from good

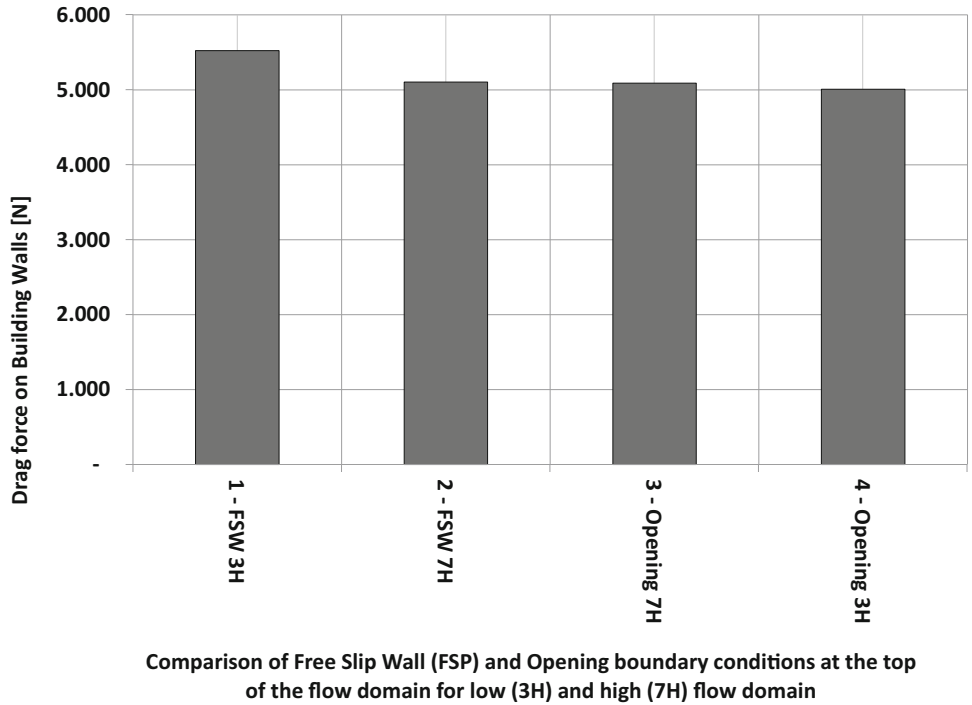


Fig. 11 Drag force on building for 3H and 7H flow domain height with free slip wall and opening boundary conditions

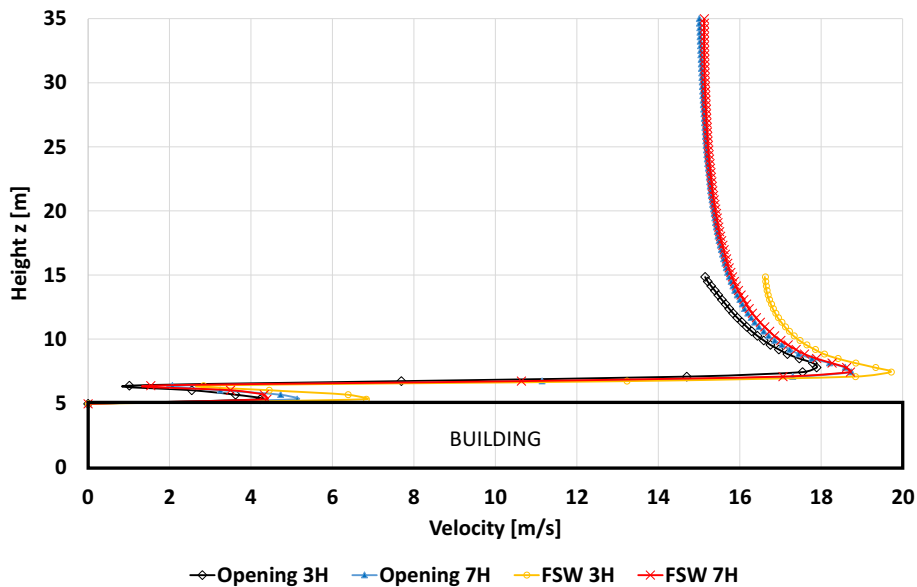


Fig. 12 Velocity profile above the center of the building

to excellent. Considering the complexity and the size of the grid the overall quality of the grid can be considered outstanding.

The  $y^+$  values on the roof of Building 4 were all below 30 and, hence, in the lower logarithmic law region—mainly in the buffer layer and in the viscous sublayer regions. Due to the complexity and size of the grid (>28 million elements), the region near the wall already had a very high resolution. The building surfaces with their many small details and steps caused difficulties in the grid generation. However, keeping these details was considered important, since the aim of this work was to

employ the building’s actual geometry, as obtained by the laser scanning, to generate highly realistic numerical results.

### 3.7 Boundary conditions and setup

The boundary conditions are shown in Fig. 18. A velocity boundary condition was specified, at the inlet. At the top, left, right, and the outlet, a pressure boundary condition, which is called an “opening” in ANSYS CFX, was specified. The outlet boundary condition allowed for both outflow and inflow, in case there was any back-



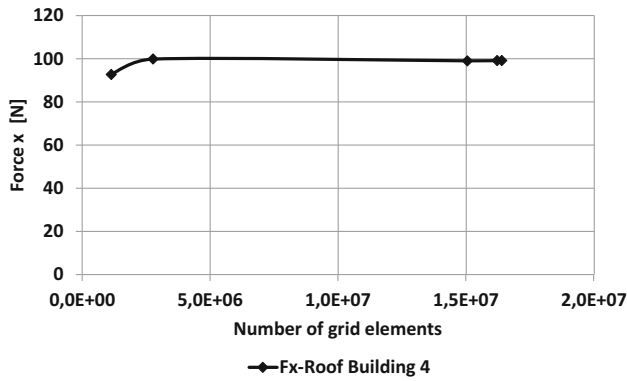


**Fig. 13** Grid convergence—Force on roof of Building 4 with 5 of the 30 tested grid results shown

**Table 1** Grid element sizes

Location	Mesh size [m]	Prism layers	Comments
Buildings	0.2	30	For Buildings 4 and 6
Ground between buildings	0.2		
General inner	1.2	30	
General outer	3.0	30	

flow into the flow domain. At the ground and on the surface of the buildings, a no slip wall condition was specified. The buildings were computed as having smooth walls. The inner and the outer grounds were computed as smooth walls, as well. Between the inner and the outer grids, general grid interfaces were specified.

The inlet velocity profile was specified according to Eq. 4 where  $z_0 = 2\text{ m}$ ,  $z_1 = 80\text{ m}$  and  $u(z_1) = 13\text{ m/s}$  were selected as inputs according to the measured wind data:

$$\begin{aligned}
 u_{\log}(z) &= u(z_1) \frac{\ln(z/z_0 + 1)}{\ln(z_1/z_0)} \\
 &= 13 \frac{\ln(z/2 + 1)}{\ln(80/2)} \text{ in (m/s)} \quad (12)
 \end{aligned}$$

This equation was derived according to the wind velocity measurements. The measured velocity at a height of  $z_1 = 80\text{ m}$  was  $u_1 = 13\text{ m/s}$  and at a height of  $z_2 = 10\text{ m}$  was  $u_2 = 6,31\text{ m/s}$ . With these two measured velocities inputted into Eq. (4) the value of  $z_0 = 2\text{ m}$  was determined, resulting in Eq. (12). This equation was set as the inlet velocity using an expression in ANSYS CFX.

The Shear Stress Transport (SST) turbulence model from Menter [28] was used for the simulations. The model solves a turbulence/frequency-based  $k-\omega$ -model at the wall and a  $k-\varepsilon$ -model in the bulk flow, while smooth transitions between the two models are achieved by a blending function. Among the RANS turbulence models, the SST  $k-\omega$  model generates the closest match to experimental data in terms of mean velocity vector fields and turbulent kinetic energy contours [29]. Additionally, this model effectively represents the kinetic energy from turbulence. Additionally, the model includes transport effects of the eddy-viscosity to accurately predict the onset and size of the flow separation under adverse pressure gradients. These combine to enable results in improved prediction of the flow separation, which is critical for the study of building aerodynamics [25].

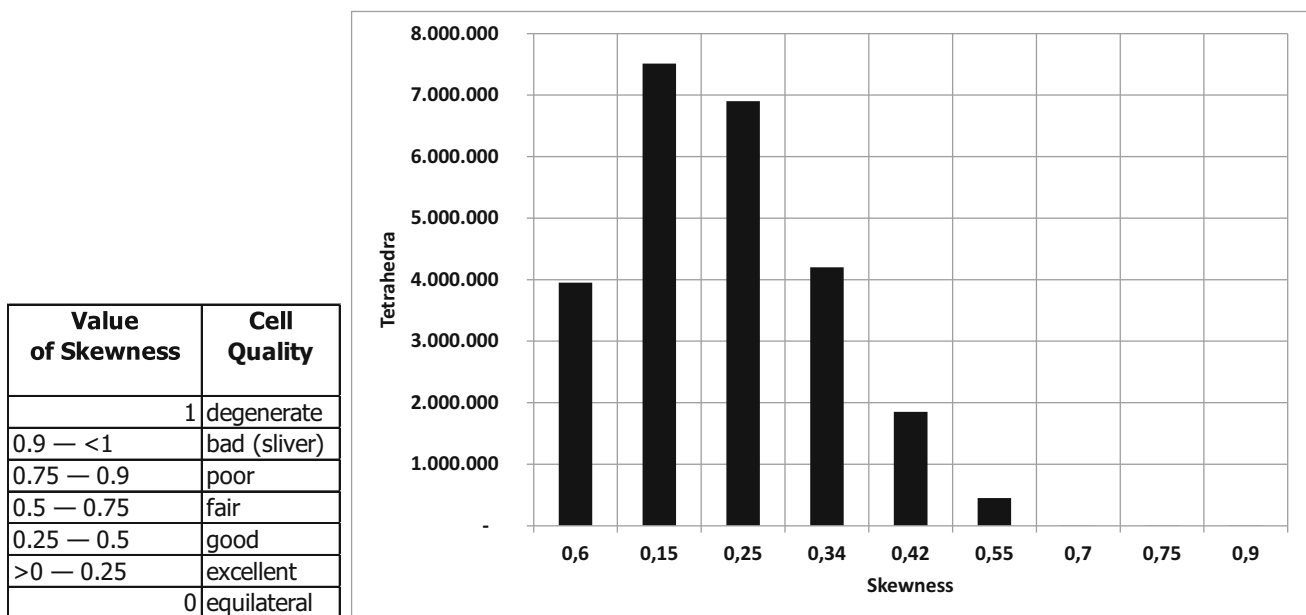


**Fig. 14** Skewness of the tetrahedral grid

**Fig. 15** Grid sizes on the buildings and on the inner and outer domains

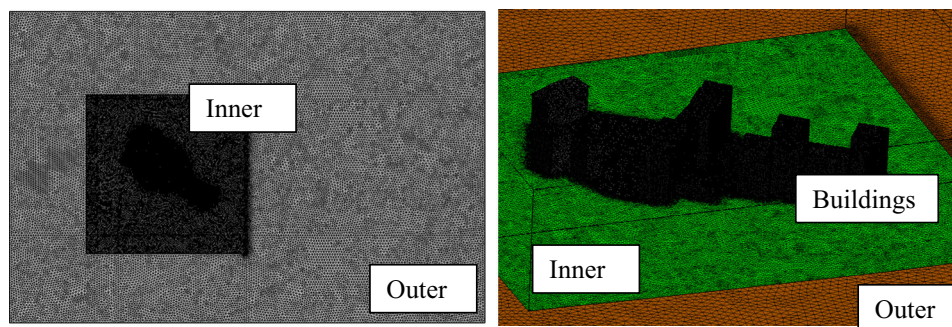


**Fig. 16** Inner and outer domain grids and the corresponding prism layers on the ground

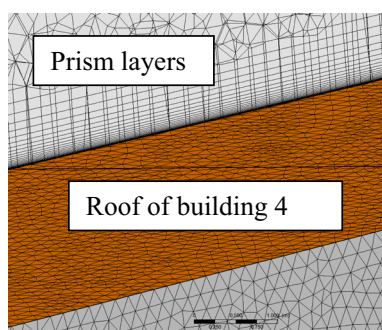
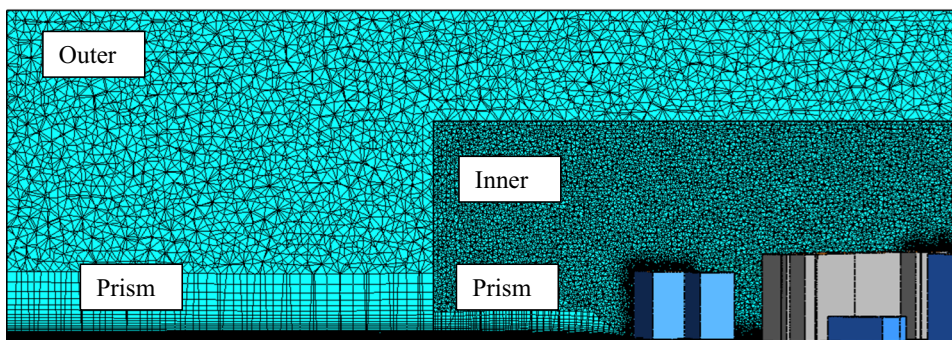


**Fig. 17** Prism layers on the roof of Building 4

Importantly, van Hooff et al. [29] conducted a detailed study comparing the performance of RANS and LES turbulence models in building aerodynamics. That work showed that Re-normalization Group (RNG) and SST are the best performing RANS turbulence models. In addition, Ramponi and Blocken [14, 30] analyzed the performance of the standard  $k-\varepsilon$  model, realizable  $k-\varepsilon$  model, RNG  $k-\varepsilon$  model, standard  $k-\omega$  model, SST  $k-\omega$  model, and a RSM model when modeling the mean streamwise velocity through the center of the two symmetrically positioned windows. In evaluating the mean velocity vector fields against the corresponding measured values, the SST  $k-\omega$  model matched the measured values most closely, while the RNG  $k-\varepsilon$  model provided the second-best results [30]. Those efforts provided the basis for selecting an SST based model in the study herein.

The convergence criteria of the CFD simulations were a combination of three factors: residuals, mass flow balance, and a steady solution of the integral value of

interest. The convergence criteria for the mass flow and momentum residuals were both  $10^{-4}$ , which are the recommended values of ANSYS CFX and, as such, also the standard setting of the solver. The mass flow balance was also observed during simulation, thereby assuring that the mass flow in the flow domain was the same as that flowing out of the domain. This was achieved very precisely, as described in the next section. The simulation was terminated when the drag forces on the six buildings ceased changing and reached a steady solution as recommended by Ferziger and Peric [31] and Tominaga et al. [32].

### 3.8 Wind velocity and normalized wind velocity

To measure the influence of the buildings on the air flow, a normalized velocity was considered. The normalized velocity used in this study was defined as the ratio of the wind velocity to the logarithmic velocity, as per the following equation:

$$u_{norm}(z) = \frac{u(x, y, z)}{u_{log}(z)}. \quad (13)$$

Herein, the logarithmic velocity  $u_{log}(z)$  was set as a boundary condition at the inlet of the flow domain. If instead there were no buildings, then the normalized velocity  $u_{norm}(z)$  should be close to the value 1 across the whole flow domain, since the flow would be nearly undisturbed, but for the effect of the boundary layer. As is well-established [27] the boundary layer thickness of a flat plate does increase continuously. This means that even without buildings, the wind velocity changes close to the ground. When, however, the buildings are

present, the air velocity may deviate significantly from the logarithmic velocity due to the displacement effect of the buildings.

### 3.9 Wind power density and normalized wind power

The wind power density can be derived directly from Eq. 7

$$P_{density} = \frac{dP_{wind}}{dA} = \frac{1}{2}\rho u(z)^3 \text{ in W/m}^2 \quad (14)$$

and the normalized dimensionless wind power is as per the following equation:

$$P_{norm} = \frac{P_{Density}}{\frac{1}{2}\rho u_{log}(z)^3} = u_{norm}(z)^3. \quad (15)$$

With wind power density, an estimate of the power generated by an RIWT is possible. If the variability of the wind is to be considered a Rayleigh wind distribution can be assumed and the results have than to be multiplied by a factor of  $6/\pi$  as has been shown in Eq. (11). The normalized wind power shows the buildings' influence on the undisturbed flow.

## 4 Results

To evaluate the urban surroundings as to available wind energy, relevant new variables were defined. The results presented below show that the wind velocity, the normalized wind velocity, the normalized wind power, and the wind power density are suitable variables to analyze the available wind power in the near vicinity of buildings.

### 4.1 Wind velocity and normalized wind velocity

To understand the information given by the normalized velocity, three contour plots are shown in Fig. 19. Figure 19a shows the actual wind velocity around the buildings. Figure 19b displays the logarithmic velocity with an inlet boundary condition. Notably, the velocity does not change around the buildings, since it is used as a boundary condition at the inlet and only as a reference velocity. Figure 19c illustrates the normalized velocity. This is the ratio of the velocity to the logarithmic velocity. The normalized velocity is smaller than 1 in areas where the computationally predicted velocity is smaller than the logarithmic velocity (used to predict the unimpeded flow) and greater than 1 in areas where the computationally predicted velocity exceeds the logarithmic velocity. For example, in Area A, the velocity is lower than the logarithmic velocity. Hence the normalized velocity is smaller than 1. In contrast, in Area B the velocity is higher than the logarithmic velocity, and hence the normalized velocity is larger than 1. Figure 19c indicates that for nearly all critical locations

for RIWT placement the logarithmic approach over-predicts the wind velocity, and that the actual wind velocity, if not zero, is nearly negligible with respect to its potential for effective RIWT placement.

Of further note is that in Area B the velocity is higher than the logarithmic velocity due to the presence of the buildings. The streamlines are curved, and high velocities from higher areas are bent downwards towards the ground. Therefore, the normalized velocity is an indicator of areas where the flow velocity is higher or lower than the undisturbed flow (based on the logarithmic prediction), which is important for RIWT placement selection. A side view of the normalized velocity is shown in Fig. 20.

In Fig. 21, the normalized velocity is shown at a height of  $z=4\text{m}$ . Just in front of the buildings and between them, the velocity is often much higher than the undisturbed incoming flow, which may cause pedestrian wind comfort problems due to increased wind velocity. On the leeward side of the building group, there is a substantial area where the normalized velocity is higher than 1. The explanation for this area is the same as for Area B in Fig. 19b [i.e., the presence of the buildings bends high velocity flows from higher elevation positions groundward, as clearly seen in the section of the scene (Fig. 20)].

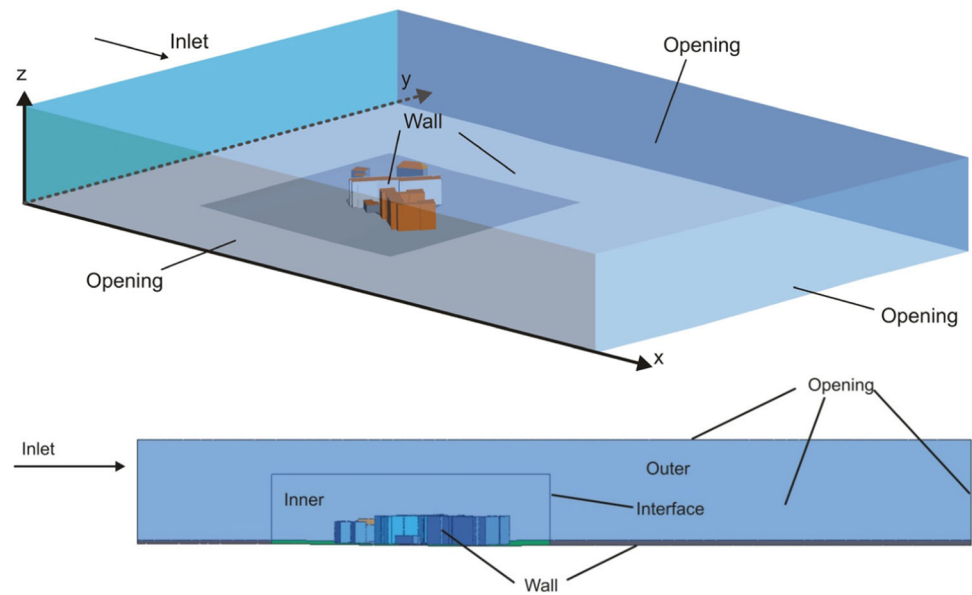
In Fig. 22, the normalized velocity is shown at a height of  $z=23.1\text{ m}$ , which is 2 m above the roof of Building 4 (see also Fig. 22 and shown in detail in Fig. 23). Red areas atop the buildings are areas where the velocity exceeds that which would be there without the buildings and are indicative of potentially good locations for RIWT placement.

As shown in Fig. 23, such areas occur only at selected locations above Buildings 4 and 6 (see red patches on the roofs). Fig. 24 demonstrates the acute difficulty of RIWT placement selection. In this image, the distance between the grey horizontal lines in this contour plot is 1 m. From the horizontal lines and the contour plot, one can see by counting the lines that the outer velocity (i.e., the undisturbed flow velocity) is reached only at heights of 2 m–8 m above the roof. In some roof regions, even at heights of more than 3 m there is still almost no wind velocity (see Area A). Therefore, RIWT placement on Building 4 would have to be carefully studied with respect to unit mounting and wind orientation to achieve a financially viable investment. As only one specific inflow wind direction was considered in this study, this represents only a mean direction according to the wind rose from the weather data of that neighborhood. A fully exhaustive study from all directions would be needed to obtain the peak velocity, but for the main case of available RIWT power studied herein, the mean inflow from the mean direction provides a strong indication of the available wind resource.

### 4.2 Wind power density and normalized wind power

Figure 25 shows the wind power density around Building 4. For most of the roof region up to about 2 m above

**Fig. 18** Boundary conditions and interface



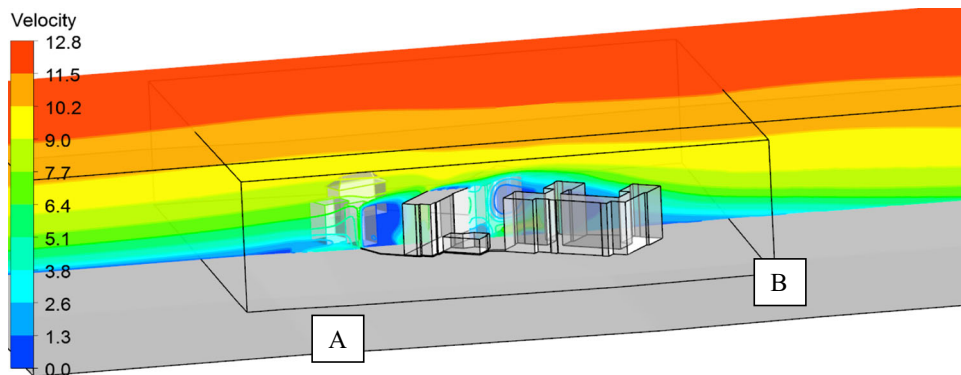
and especially in Area A, the power density is comparatively low. Only at a distance of about 6 m over the roof is the wind power density close to the value of the undisturbed wind. This can also be seen in the normalized wind power plot in Fig. 26. The normalized power plot shows how much the wind power is changed by the presence of the buildings. Values above 1 indicate that the presence of the building increases the available power at this location, as compared to the power that would be available in the undisturbed flow (i.e., if the building were not standing there). Values below 1 identify power availability less than under the undisturbed flow condition at that location. As can be seen in Fig. 26, power availability on the building's roof is generally lower compared to the undisturbed flow, but there are exceptions such as the far right above Building 4.

In Fig. 27, the energy per year and per square meter for Building 4 is presented. These values were computed by multiplying the values of Fig. 26 by  $8.760 = 24 \times 365 / 1000 = 8760 / 1000$  since a year has 8760 h. The division by 1,000 obtains the result in kWh instead of Wh per year. As such, the energy that can be generated by a RIWT can be estimated with this figure. For example, if the RIWT has a rotor area of  $20 \text{ m}^2$  and an efficiency of 50%, by multiplying the values of the contour plot by  $20 \times 0.5 = 10$  one obtains a rough estimation of the power output of such a RIWT. Considering also the wind oscillations according to the Rayleigh distribution this result must still be multiplied by a factor of  $6/\pi$  (see Eq. 10). In Fig. 28 the vorticity around Building 4 is shown. The regions of high vorticity basically coincide with the regions of flow detachment and, hence, of recirculation.

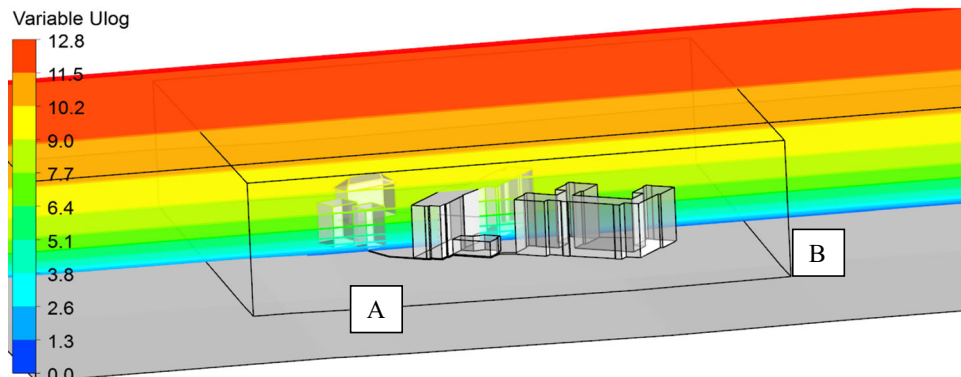
Figures 29 and 30 show the wind power density across all 6 buildings at a height of  $z=23.1 \text{ m}$  (i.e., 2 m above the roof of building 4 level). In many locations, the wind power density is quite low and may prove financially non-viable for RIWT investment.

In Fig. 30, the surrounding buildings' influence on the available wind power density is shown. Overall, the buildings retard the wind and create a de facto low velocity "bubble" around the buildings. Atop the buildings, the wind power density is also reduced, as compared to the incoming free stream flow. Therefore, to set a small scale RIWT atop a building may provide few advantages, unless carefully situated. Across the 7 representative small wind turbine models considered by Cace et al. [33] for installation in the built environment, prices ranged from an estimated €5700 to over €24,000 with a median cost of €16,500. For the normalized wind example provided in Fig. 30, if the RIWT was mounted within the immediate proximity of the roof (from 0 to 2 m above the roof's surface), the estimated yearly power production at the most optimal position on the roof would be 168,750 kWh for an average 5 m diameter turbine with a blade surface area of  $19.6 \text{ m}^2$  costing €16,500. Based on a market value of €0.1297/kWh [33,34], this would require less than 1.3 years to recover costs for the RIWT. The same device placed at the same elevation elsewhere on the same roof, however could end up in an area of 0–500 kWh/m<sup>2</sup> wind power density producing only a maximum of 11,091.33 kWh of energy per year and, thus, requiring over 11 years to recoup initial costs.

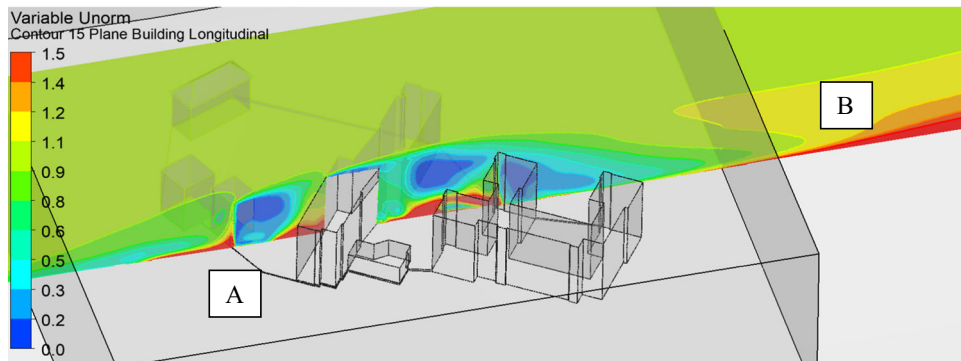
A closer view of this situation can be seen in Fig. 31. Here the low wind power density "bubble" is visible up to about 5 m over the building roofs. Mounting a small-scale RIWT on a tower sufficiently high to keep the wind turbine out of this 5 m low wind power density area will enable it to reach a much higher wind power density area, even when compared to a ground-based tower of the same height in the undisturbed wind. As can be seen from these results, RIWT installation locations must be thoughtfully selected, since (as demonstrated with Building 4) the wind power availability changes substantially depending on the placement.



(a) Computationally predicted wind velocity



(b) Logarithmic-based wind velocity as predicted by standard theory



(c) Ratio of logarithmic to computational outputs highlighting the differences in the methods

Fig. 19 Comparison of estimated wind velocities based on computational modeling and empirical approaches

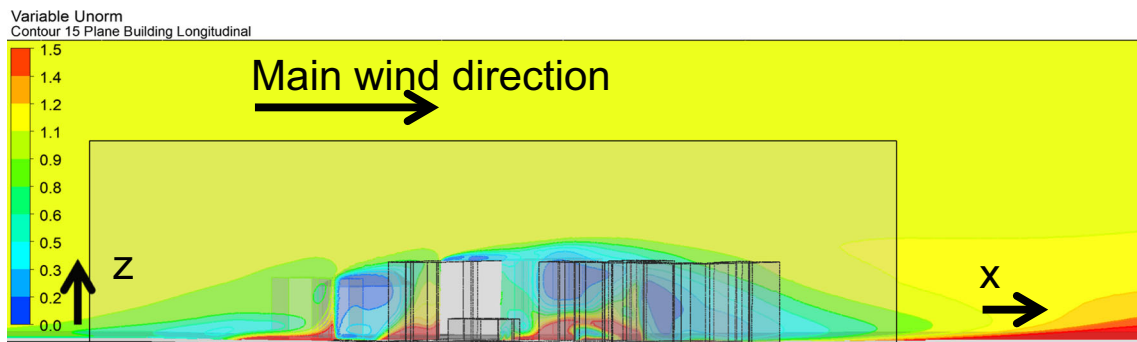
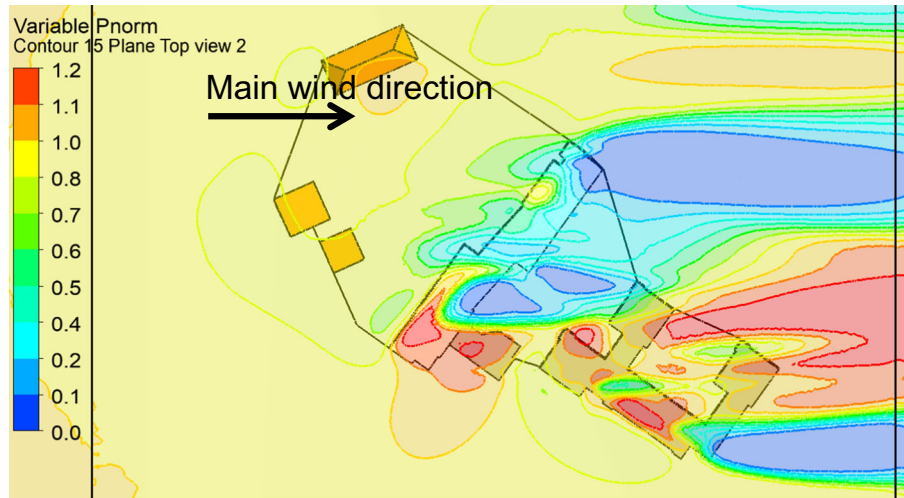
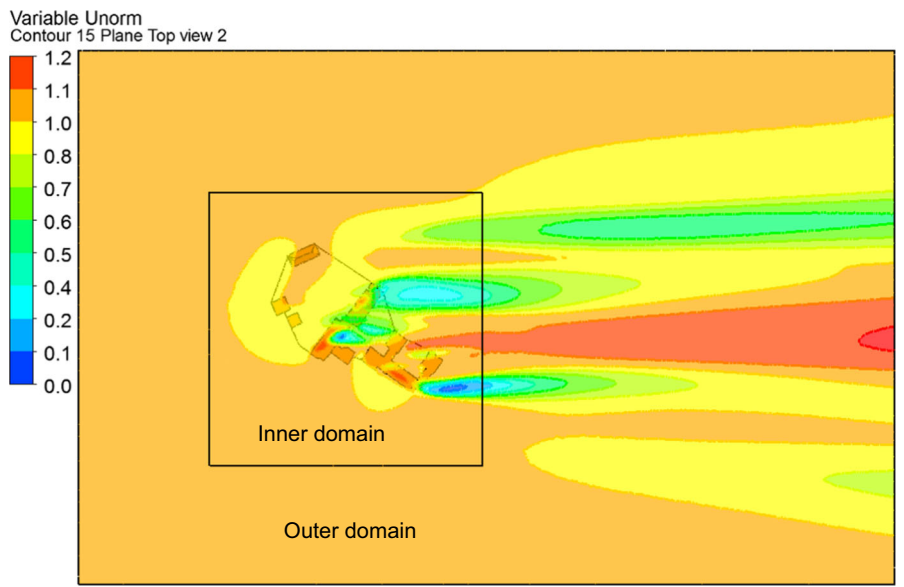


Fig. 20 Scene section of the effect of the buildings on the wind showing the normalized velocity of Eq. 13



**Fig. 21** Normalized velocity at  $z=4$  m



**Fig. 22** Normalized velocity at  $z=23.1$  m

### 4.3 Pedestrians

A related issue when analyzing wind flow around buildings is pedestrian wind comfort. The simulation presented above for wind production estimation can also be used for pedestrian wind comfort prediction as shown in Fig. 32. As is known from the fundamentals of fluid mechanics [27], when a fluid flows around a cylinder, the velocity close to the cylinder accelerates to as much as twice the free stream velocity. Similar behavior occurs with the flow around buildings. Although this contour plot is at  $z=4$  m, it corresponds to a height from the ground of around 2 m, as can be seen when compared with Fig. 8. In Fig. 32, several spots of high velocities can be seen, as for instance in A, B, C and D, which might be critical for pedestrian comfort.

### 4.4 Aerodynamic forces on the buildings

Another result from the CFD computations is the group of forces acting on the buildings, as required for structural design. For example, in Fig. 33 the lift force (i.e., the vertical force in  $z$  direction, which is perpendicular to the oncoming flow direction [35, 36] on the buildings is shown. At the vertical walls, there is almost no lift. However, the lift on the roofs is substantial, irrespective of geometry [i.e., gabled (Building 1) or flat (all others)].

In Fig. 34, the horizontal forces on the buildings are shown. On the roof of the building there is almost no horizontal force, but the horizontal forces are quite substantial on the facades and might represent important input information for structural design. Notably, all the necessary information on forces and pressure distribu-

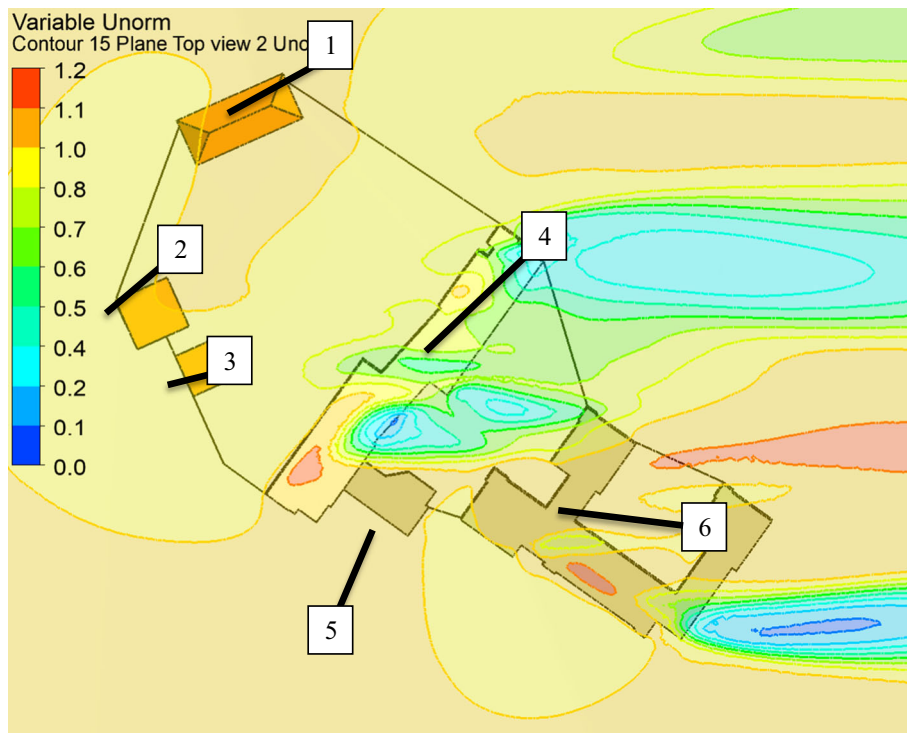


**Fig. 23** Detailed view over the buildings of the normalized velocity at  $z=23.1$  m

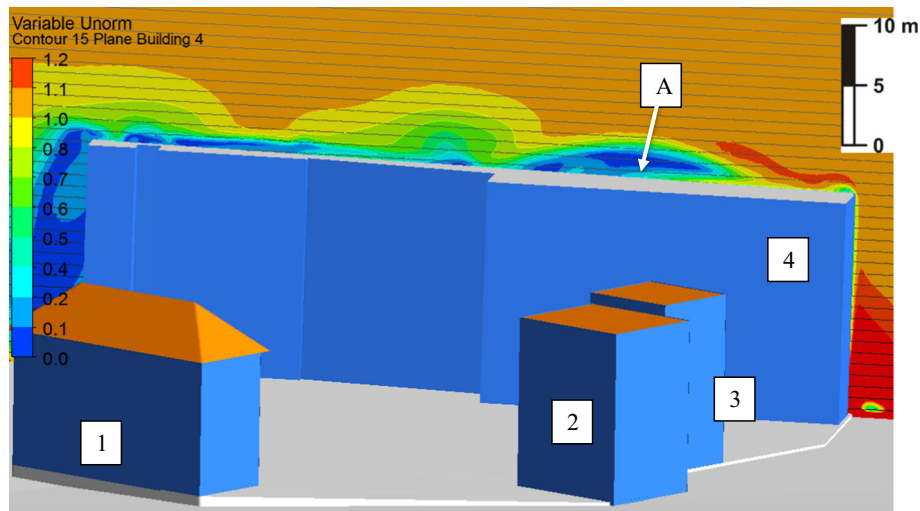


**Fig. 24** View of the normalized velocity around Building 4

tions on the roofs and facades may be obtained from the CFD results. These results generally indicate the need for better wind models and highly precise geometry for modeling both the building in question and the surrounding structures, as previously highlighted [37,38].

### 5 Conclusions

In this work, a CFD analysis approach was applied to explore the possible reasons for the typically dis-

appointing performance of urban RIWTs and potential mitigation strategies. As a case study for this analysis, a complex real-world geometry of a building, its surrounding structures, and changes in ground eleva-

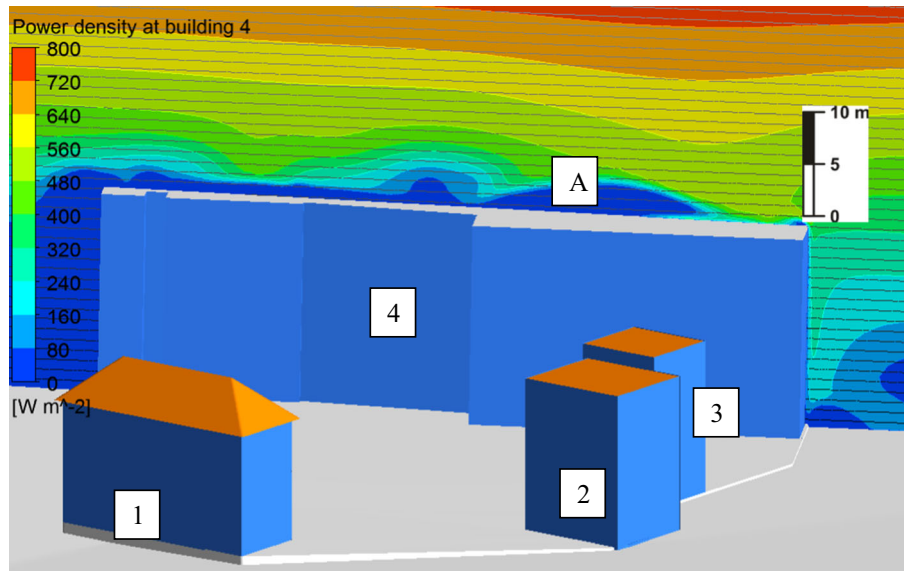


**Fig. 25** Predicted power density around Building 4

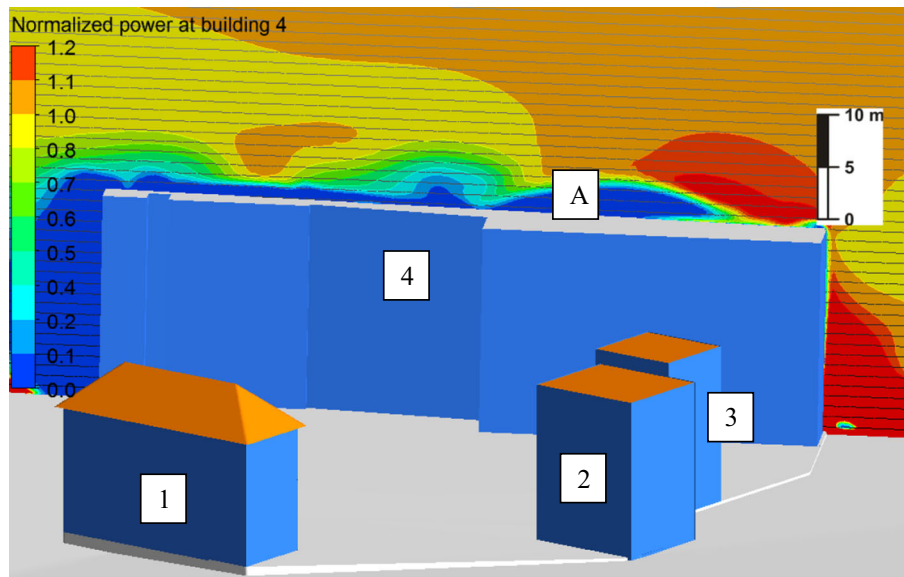


**Fig. 26** Normalized wind power

tion from - 1.4 m to + 208 m were obtained by terrestrial laser scanning. Based on these data, a CFD simulation was conducted to provide information about the wind power likely to be available based on the definition and usage of the wind velocity, the wind velocity, the normalized wind velocity, the normalized wind power, and the wind power density as input variables. These enabled a detailed analysis of projected wind power available for RIWT usage across the entire roof in question. The output showed variations of 0 to 4500 kWh/m<sup>2</sup> per year at 2 m above the roof, a difference between non-viability and complete cost recovery in less than 1.5 years for a €16,500 RIWT. This work also found that an elevation of 5 m above the roof is needed to harvest unimpeded wind flow. Thus, past

failures of RIWTs appear to have been more related to installation location than the devices themselves, and that employment of terrestrial laser scanning can economically provide the necessary input data to achieve a sufficiently accurate wind model for financially viable RIWT placement. This was demonstrated on a real-world structure of significantly greater complexity than is usually considered. Thus, importantly, this approach addresses real world issues of multi-building complexes and changes in ground elevation to which overly simple models and modeling rules are not applicable. Furthermore, the paper demonstrates that CFD implemented upon highly realistic building geometry is not only a powerful tool to investigate the best installation location for RIWTs in a complex urban environment but



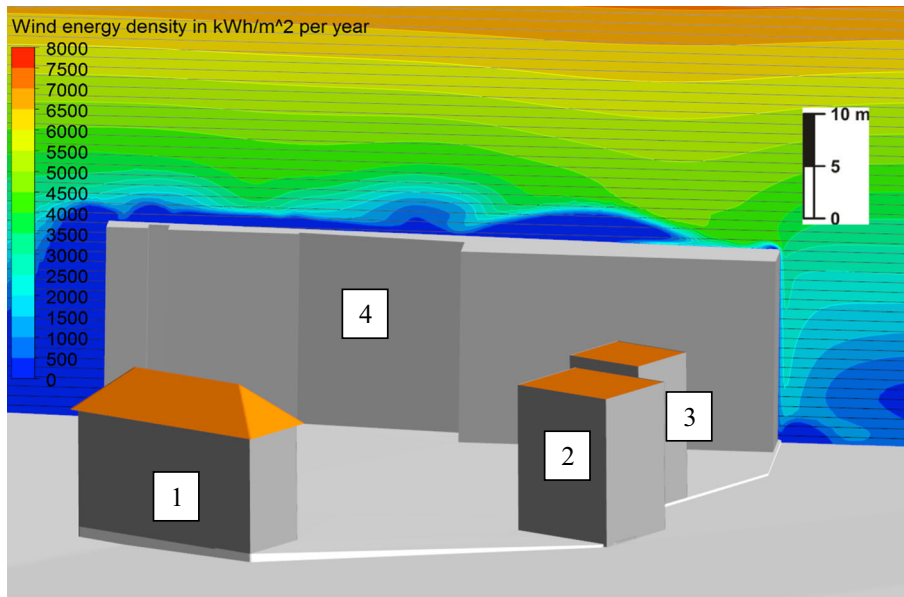


Fig. 27 Wind energy density per year

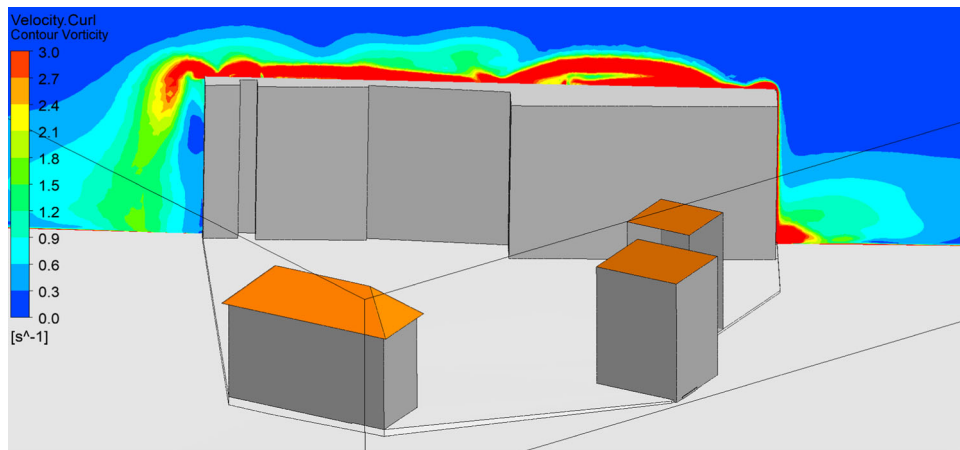
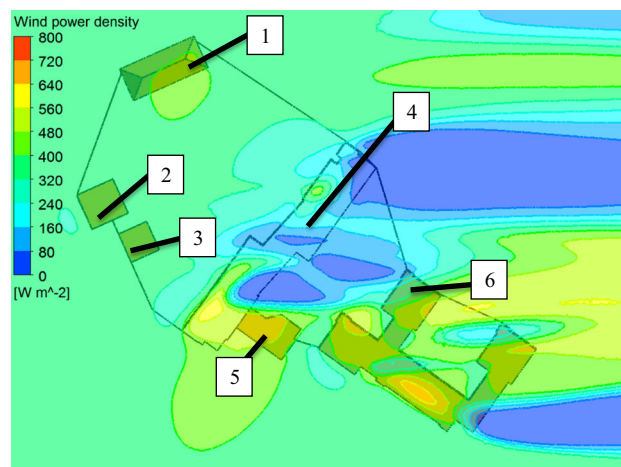


Fig. 28 Vorticity around Building 4

Fig. 29 Wind power density at z=23.1 m height



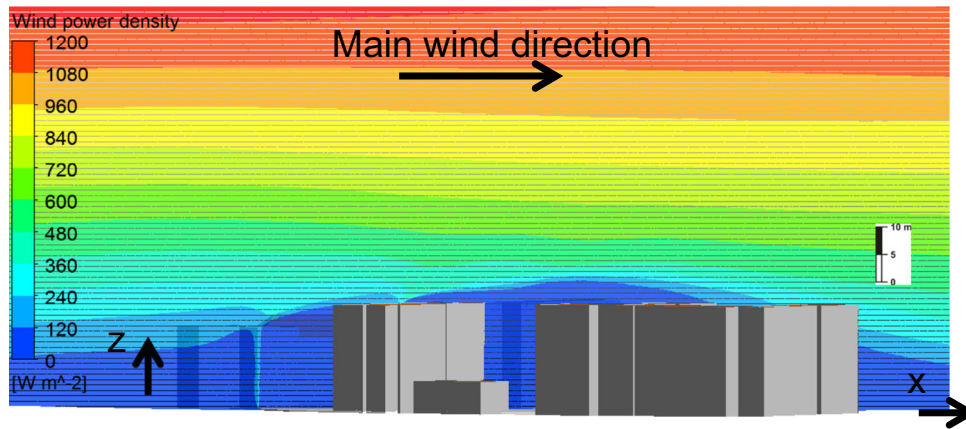


Fig. 30 Wind power density side view

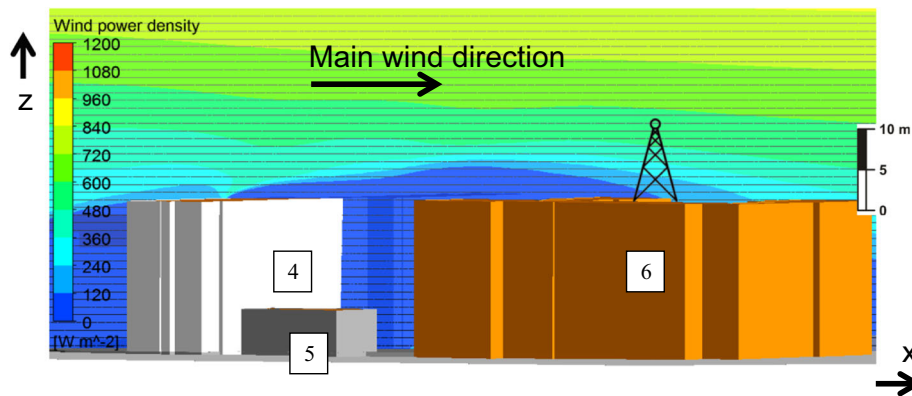


Fig. 31 Wind power density close to Buildings 4, 5 and 6

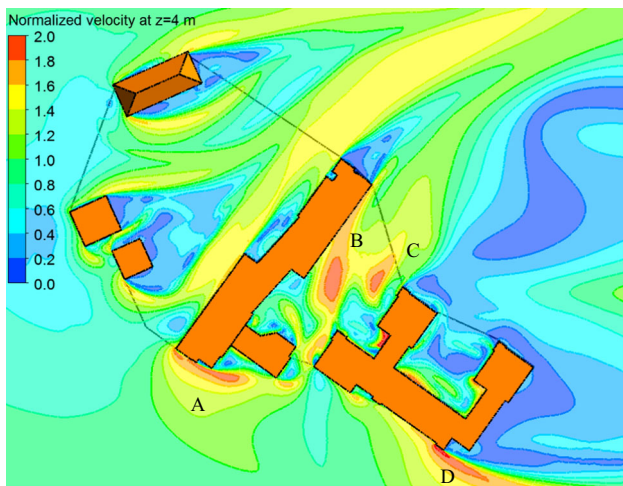


Fig. 32 Normalized velocity at a pedestrian height

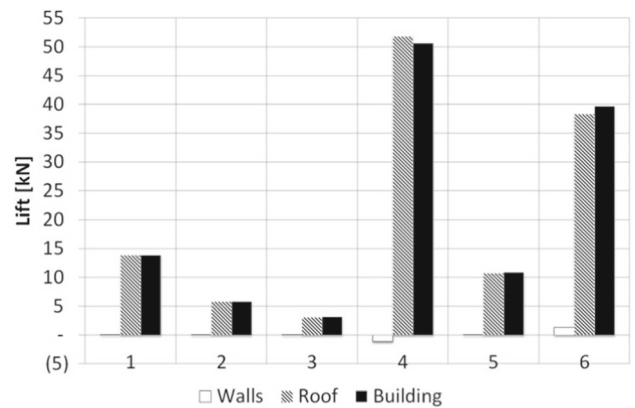


Fig. 33 Lift force on buildings

also a valuable tool for other applications such as wind force estimations to inform the structural design of buildings and pedestrian wind comfort analysis.

**Acknowledgements** The authors are grateful for the technical assistance provided by Donal Lennon and funding through the European Union FP7 ERC grant 307836,

H2020 European Research Council, ERC StG 2012-307836-RETURN.

### Author contribution statement

Gitanjali Thakur conceived the study and collected historical and field data, and performed the initial simulation. Philipp Epple oversaw and improved the numerical simulation with contributions from Gitan-

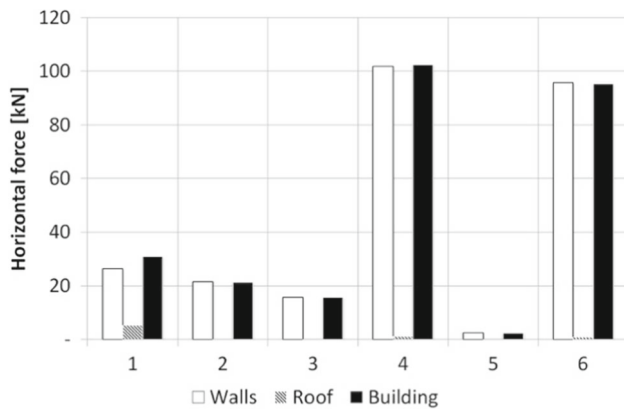


**Fig. 34** Horizontal force on buildings

jali Thakur, Debra Laefer coordinated and oversaw the project, as well provided equipment and other financial resources. All the authors contributed extensively to the writing, editing, and revision of the paper.

### Declarations

**Competing interests** The authors have no financial or non-financial interests that are directly or indirectly related to the work submitted for publication.

### References

1. A. Zygierewicz, L. Salvador Sanz, Renewable Energy Directive. *European Parliamentary Research Service*. <https://euagenda.eu/upload/publications/eps-bri2021662619-en.pdf>, (Mar 2021)
2. Encraft. *Warwick Wind Trials Report* [http://www.microwindturbine.be/Rapportering\\_files/Warwick+Wind+Trials+Final+Report+\(1\).pdf](http://www.microwindturbine.be/Rapportering_files/Warwick+Wind+Trials+Final+Report+(1).pdf) (2009)
3. S.L. Walker, Building mounted wind turbines and their suitability for the urban scale—a review of methods of estimating urban wind resource. *Energy Build* **43**, 1852–1862 (2011)
4. A. Al-Quraan, T. Stathopoulos, P. Pillay, Comparison of wind tunnel and on site measurements for urban wind energy estimation of potential yield. *J Wind Eng Ind Aerodyn* **158**, 1–10 (2016)
5. K.M. Sunderland, G. Mills, M.F. Conlon, Estimating the wind resource in an urban area: A case study of micro-wind generation potential in Dublin. Ireland. *J Wind Eng Ind Aerodyn* **118**, 44–53 (2013)
6. G. Falcucci, G. Amati, Ps. Fanelli et al., Extreme flow simulations reveal skeletal adaptations of deep-sea sponges. *Nature* **595**, 537–541 (2021)
7. P. Larin, M. Paraschivoiu, C. Aygun, CFD based synergistic analysis of wind turbines for roof mounted integration. *J Wind Eng Ind Aerodyn* **156**, 1–13 (2016)
8. L. Ledo, P.B. Kosasih, P. Cooper, Roof mounting site analysis for micro-wind turbines. *Renew Energy* **36**(5), 1379–1391 (2011)
9. F. Balduzzi, A. Bianchini, L. Ferrari, Microeolic turbines in the built environment: Influence of the installation site on the potential energy yield. *Renew Energy* **45**, 163–174 (2012)
10. A.S. Yang, Y.M. Su, C.Y. Wen, Y.H. Juan, W.S. Wang, C.H. Cheng, Estimation of wind power generation in dense urban area. *Appl Energy* **171**, 213–230 (2016)
11. B. Wang, L.D. Cot, L. Adolphe, S. Geoffroy, J. Morchain, Estimation of wind energy over roof of two perpendicular buildings. *Energy Build* **88**, 57–67 (2015)
12. I. Abohela, N. Hamza, S. Dudek, Effect of roof shape, wind direction, building height and urban configuration on the energy and positioning of roof mounted wind turbines. *Renew Energy* **50**, 1106–1118 (2013)
13. R. Gasch, J. Twele, *Windkraftanlagen*, 8th edn. (Weisbaden, Springer-Vieweg, 2013)
14. R. Ramponi, B. Blocken, L.B. de Coo et al., CFD simulation of outdoor ventilation of generic urban configurations with different urban densities and equal and unequal street widths. *Build Environ* **92**, 152–166 (2015)
15. Y. Tominaga, B. Blocken, Wind tunnel experiments on cross-ventilation flow of a generic building with contaminant dispersion in unsheltered and sheltered conditions. *Build Environ* **92**, 452–461 (2015)
16. G.M. Masters, *Renewable and Efficient Electric Power Systems*. Hoboken, NJ, (Wiley Interscience, 2004)
17. A. Betz, *Introduction to the Theory of Flow Machines*. 1st Eng. London: (Pergamon Press, 1966)
18. A.N. Celik, A statistical analysis of wind power density based on the Weibull and Rayleigh models at the southern region of Turkey. *Renew Energy* **29**, 593–604 (2004)
19. J.V. Seguro, T.W. Lambert, Modern estimation of the parameters of the Weibull wind speed distribution for wind energy analysis. *J Wind Eng Ind Aerodyn* **85**, 75–84 (2000)
20. R.I. Harris, N.J. Cook, The parent wind speed distribution: Why Weibull? *J Wind Eng Ind Aerodyn* **131**, 72–87 (2014)
21. T. Arslan, Y.M. Bulut, Yavuz A. Altın, Comparative study of numerical methods for determining Weibull parameters for wind energy potential. *Renew Sustain Energy Rev* **40**, 820–825 (2014)
22. K. Mohammadi, O. Alavi, A. Mostafaeipour et al., Assessing different parameters estimation methods of Weibull distribution to compute wind power density. *Energy Convers Manag* **108**, 322–335 (2016)
23. J. Franke, A. Hellsten, H. Schlünzen et al. (eds.), *Best practice guideline for the CFD simulation of flows in the urban environment: Action 732* (COST, Brussels, 2007)
24. Leica Geosystems. *Leica ScanStation P20 Industry's Best Performing Ultra-High Speed Scanner [Datasheet]*. (2013)
25. Leica Geosystems AG. Leica Cyclone Verarbeitungssoftware für 3D-Punktwolken <http://leica-geosystems.com/de-de/products/laser-scanners/software/leica-cyclone>. Accessed 2 (May 2017)
26. Leica Geosystems AG. Leica Cloudworx Produktfamilie <http://leica-geosystems.com/de-de/products/laser-scanners/software/leica-cloudworx>. Accessed 1 (May 2017)
27. Y. Tominaga, A. Mochida, R. Yoshie et al., AIJ guidelines for practical applications of CFD to pedestrian

- wind environment around buildings. *J Wind Eng Ind Aerodyn* **96**, 1749–1761 (2008)
28. FR. Menter, Zonal Two Equation  $k-\omega$  Turbulence Models for Aerodynamic Flows. In: *24th AIAA Fluid Dynamics Conference*. Orlando, p. AIAA 93-2906
  29. T. van Hooff, B. Blocken, Y. Tominaga, On the accuracy of CFD simulations of cross-ventilation flows for a generic isolated building: comparison of RANS, LES and experiments. *Build Environ* **114**, 148–165 (2017)
  30. R. Ramponi, B. Blocken, CFD simulation of cross-ventilation flow for different isolated building configurations: Validation with wind tunnel measurements and analysis of physical and numerical diffusion effects. *J Wind Eng Ind Aerodyn* **104–106**, 408–418 (2012)
  31. J.H. Ferziger, M. Peric, R.L. Street, *Computational Methods for Fluid Dynamics*, 4th edn. (Springer, Berlin, 2020)
  32. Y. Tominaga, A. Mochida, R. Yoshie, H. Kataoka, T. Nozu, M. Yoshikawa, T. Shirasawa, AIJ guidelines for practical applications of CFD to pedestrian wind environment around buildings. *J Wind Eng Ind Aerodyn* **96**, 1749–1761 (2008)
  33. J. Cace E. Horst K. Syngellakis, et al. *Urban wind turbines: Guidelines for small wind turbines in the urban environment* <http://www.urbanwind.net/>. [http://www.urbanwind.net/pdf/SMALL\\_WIND\\_TURBINES\\_GUIDE\\_final.pdf](http://www.urbanwind.net/pdf/SMALL_WIND_TURBINES_GUIDE_final.pdf) (2007)
  34. Sustainable Energy Authority of Ireland. Electricity & Gas Prices in Ireland. [http://www.seai.ie/Publications/Statistics\\_Publications/Electricity\\_and\\_Gas\\_Prices/Price-Directive-1st-Semester-2016.pdf](http://www.seai.ie/Publications/Statistics_Publications/Electricity_and_Gas_Prices/Price-Directive-1st-Semester-2016.pdf) (2016, accessed 15 July 2017)
  35. J.D. Anderson, *Fundamentals of Aerodynamics*, (McGraw-Hill Education, 5th revised ed., 2011)
  36. R. Fox, A. McDonald, P. Pritchard, *Fluid Mechanics*. 8th ed. Hoboken, (NJ: John Wiley & Sons, 2011)
  37. M. Singh, D.F. Laefer, Recent trends and remaining limitations in Urban microclimate models. *Open Urban Stud Demogr J* **1**, 1-12 (2015)
  38. D.F. Laefer, M. Anwar, Review of strategies for the geometric creation and population of Urban microclimate models. *Open Urban Stud J* **5**, 22–31 (2012)